Mind the Gap: Understanding the Modality Gap in Multi-modal Contrastive Representation Learning

Weixin Liang [*1] **Yuhui Zhang** [*1] **Yongchan Kwon** [*2 3] **Serena Yeung** [1 3] **James Zou** [1 3 4]

Abstract

We present *modality gap*, an intriguing geometric phenomenon of the representation space of multi-modal models. Specifically, we show that different data modalities (e.g. images and text) are embedded at arm's length in their shared representation in multi-modal models such as CLIP. Our systematic analysis demonstrates that this gap is caused by a combination of model initialization and contrastive learning optimization. In model initialization, we show empirically and theoretically that the representation of a common deep neural network is restricted to a narrow cone. As a consequence, in a multi-modal model with two encoders, the representations of the two modalities are clearly apart when the model is initialized. During optimization, contrastive learning keeps the different modalities separate by a certain distance, which is influenced by the temperature parameter in the loss function. Our experiments further demonstrate that varying the modality gap distance has a significant impact in improving the model's downstream zero-shot classification performance and fairness. Our code and data are available at https://modalitygap.readthedocs.io/

1. Introduction

In this work, we present the *modality gap* phenomenon: As shown in Figure 1 (b), OpenAI's CLIP's (Radford et al., 2021) image embeddings and text embeddings are located in two completely separate regions of the embedding space. We find this phenomenon consistently across various multi-modal models, covering texts, natural images, videos, medical images, and amino-acid sequences. Interestingly, this phenomenon still holds even when we embed using multi-modal models with *random* weights (Figure 1 (c)). While it might seem reasonable to attribute the gap to differences in data distributions or to the different encoder architectures, we showed that these factors are not the fundamental cause.

This paper provides a three-part explanation for the modality gap phenomenon. **(1)** The general inductive bias of deep neural architecture creates a *cone effect*: The effective embedding space is restricted to a narrow cone for pre-trained models or models with random weights. **(2)** Different random initializations create different embedding cones. Since a multi-modal model consists of two encoders, which create different cones at random initialization, this explains how the modality gap is present at initialization. **(3)** The contrastive learning objective commonly used by multi-modal models preserves the gap. We support our explanations with theory and experiments. Our theoretical analysis shows that under mild assumptions, each neural network layer shrinks the angle between any pair of embedding vectors with high probability, thereby creating more narrow cones in deeper architectures. We further prove that different random initializations of model weights result in different cones. Interestingly, increasing the modality gap in models like CLIP can improve its downstream performance on several zero-shot learning and fairness tasks. The main objective of our paper is to i) empirically demonstrate the modality gap phenomenon across different data modalities and NN architectures; ii) explain how the gap arises and iii) show that the size of the gap can affect downstream applications. It is *not* our goal to propose a method to close the gap, since it's not clear that it's desirable to have no modality gap. Together, this paper makes the **following contributions**:

1. To the best of our knowledge, we demonstrate a general *modality gap* phenomenon for the first time. We show that this phenomenon holds across a wide spectrum of multi-modal models, covering texts, natural images, videos, medical images, and amino-acid sequences.
2. We demonstrate the significant implications of modifying the gap in downstream applications. By simply modifying the gap's distance, we can improve CLIP's

[*]Equal contribution [1]Department of Computer Science, Stanford University [2]Department of Statistics, Columbia University [3]Department of Biomedical Data Science, Stanford University [4]Chan Zuckerberg Biohub, CA, USA. Correspondence to: James Zou <jamesz@stanford.edu>.

First Workshop of Pre-training: Perspectives, Pitfalls, and Paths Forward at ICML 2022, Baltimore, Maryland, USA, PMLR 162, 2022. Copyright 2022 by the author(s).

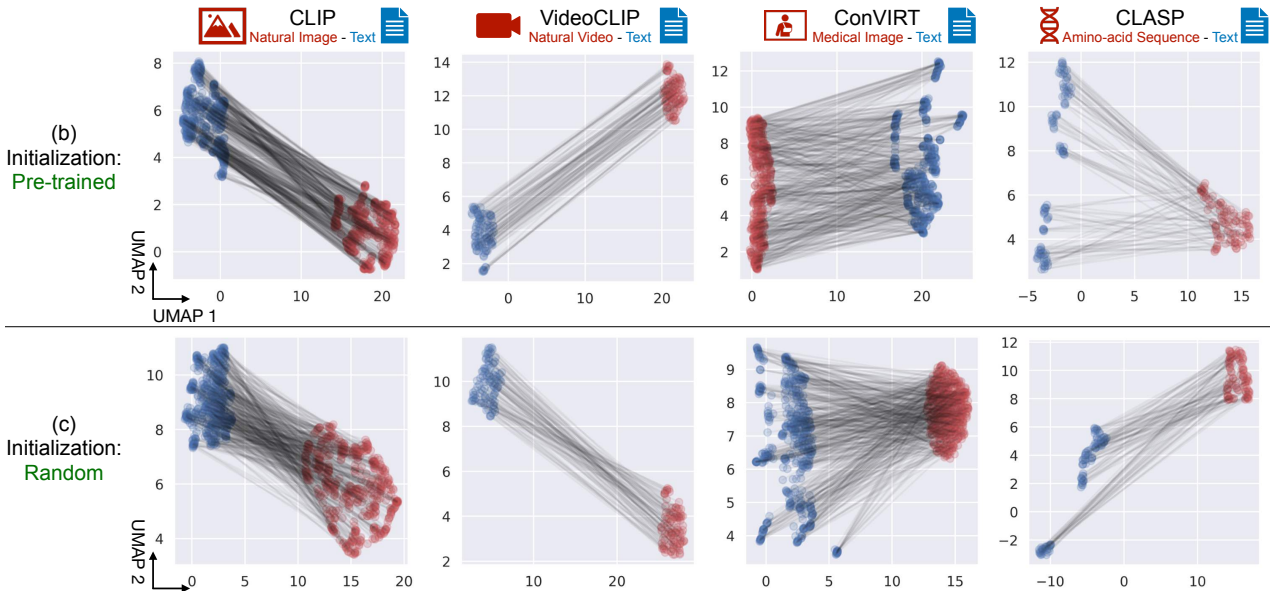

Figure 1. **The pervasive *modality gap* in multi-modal contrastive representation learning.** (b) Embeddings of paired inputs extracted from pre-trained models (lines indicate pairs). We observe a clear modality gap for various models trained on different modalities. (c) This phenomenon still holds even when we embed using multi-modal models with *random* weights.

zero-shot performance and fairness.

3. To explain modality gap, we provide a three-part explanation supported by extensive theoretical and empirical analyses. Our analyses also provide new insights on the cone effect, which we show is a general phenomenon for deep neural networks. Existing work focuses on *trained* language models and attributes the cone effect to the *optimization* under unbalanced word frequencies distribution. We demonstrate that this effect holds not only across various modalities and network architectures, but also on random noise inputs and random weights, which is not captured in previous work.
4. We mathematically characterize the contraction mapping induced by linear layers with ReLU non-linearities to explain the cone effect. Our theory matches well with experiments and provides insights for understanding the general inductive biases of deep neural networks.

2. The Cone Effect Induces A Modality Gap

2.1. The Narrow Cone of Embeddings

In order for modality gap to exist, the embeddings from a encoder should be concentrated around a subregion of the full embedding space—otherwise, the embeddings from different encoders would overlap. Motivated by this, we begin our investigation by showing that the modality gap already arises at random model initialization due to the *cone effect*: The effective embedding space is restricted to a narrow cone for trained models and models with random weights. To demonstrate this, we extract 5,000 image embeddings from ResNet and Vision Transformer, and 5,000 text embeddings from Text Transformer. We found that the cosine similarity between all possible pairs of the 5,000 embeddings within each model (Figure 2 (a)) are all positive. These results indicate that the embedding space is a narrow cone.

In the literature, the cone effect has been observed in the language representations from language models. A common explanation is that the *unbalanced* distribution of word frequencies biased the *optimization* (Gao et al., 2019). However, we found that the cone effect still exists in models with random weights (Figure 2 (c)). In fact, the average cosine similarity there is even *higher* than in trained models. For example, any two embeddings from a randomly initialized ResNet have on average an almost perfect (0.99) cosine similarity. Interestingly, the cone effect still holds when the input data is random noise, indicating that unbalanced data distribution suggested in previous works is not necessary for the cone effect. Together these experiments suggest that the cone effect reflects a more general inductive bias of deep networks than might be previously appreciated.

2.2. The effects of non-linear activation on cone effect

To study the effects of non-linear activation functions on the cone effect, we randomly initialized various MLPs with different non-linearities or without non-linearities. As shown in Figure 2 (b), MLPs without non-linear activation shows little cone effect. However, with non-linearity, the average cosine similarity increases *rapidly* as the number of

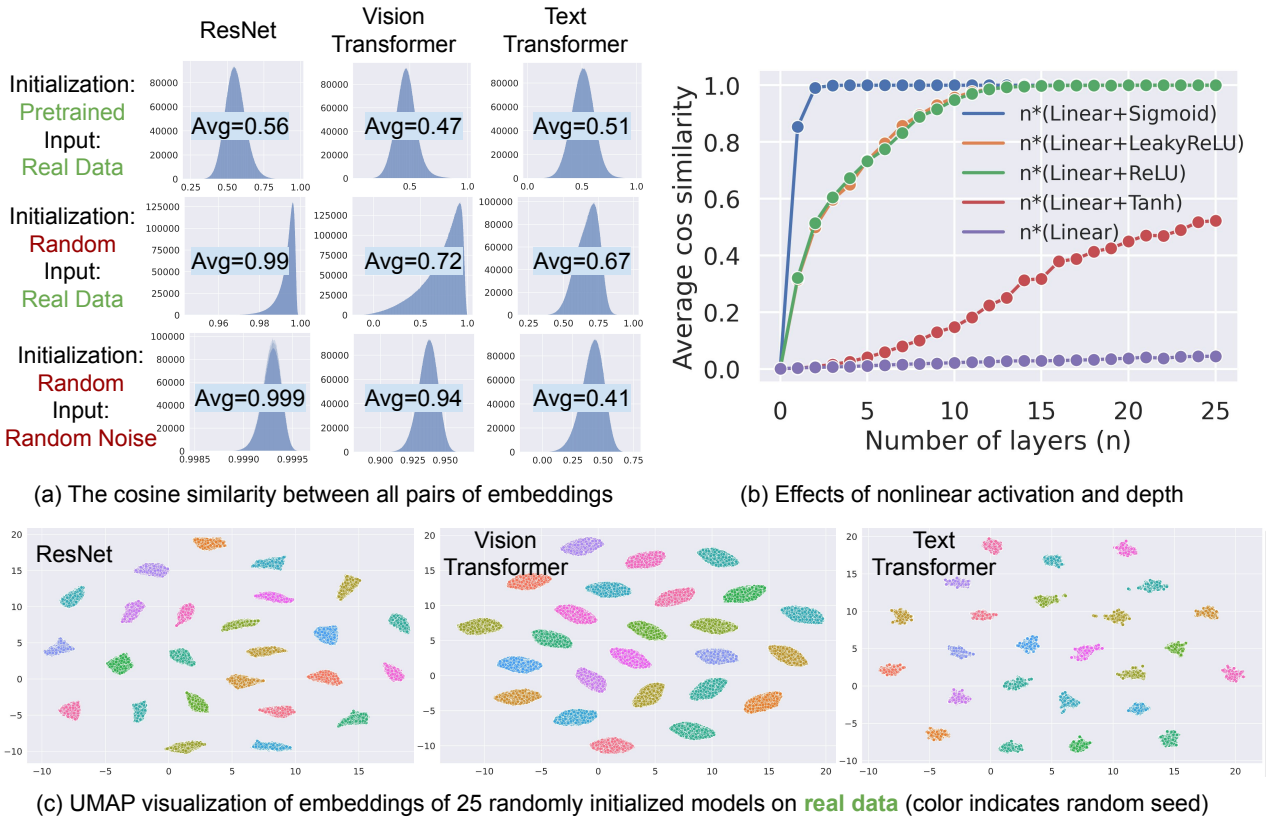

(a) The cosine similarity between all pairs of embeddings

(b) Effects of nonlinear activation and depth

(c) UMAP visualization of embeddings of 25 randomly initialized models on **real data** (color indicates random seed)

Figure 2. **The cone effect phenomenon. (a) Histograms of the cosine similarity between all pairs of embeddings across various settings.** The average cosine similarity is substantially larger than 0, indicating that the embedding space is a narrow cone. The cone effect also holds on randomly initialized models, and on random noise inputs. **(b) Effects of nonlinear activation and depth.** Inputs are 512-dim standard normal random vector. MLP weights and biases are randomly drawn from $\mathcal{N}(0, \frac{1}{512})$. **(c) UMAP visualization of embeddings of 25 models with random weights on *real* data.** Each random initialization forms a distinctively different cone.

layers increases. These results indicate that the non-linear activation functions play a crucial role in the cone effect.

2.3. Different random initializations create different cones

Next, we study the effect of different random initialization on the cone effect. In Figure 2 (c), we randomly initialized each model 25 times, and plotted its extracted embeddings on the same *real data*. We found that each random initialization forms a distinctively different cone. *While it might seem reasonable to attribute the modality gap to differences in data modalities, Figure 2 (c) shows the gap still exists even if the two encoders operate on the exact same data in the exact same modality. Therefore, the gap can exist without different modalities, and we emphasize that the modality gap phenomenon is non-trivial to understand.*

3. Theoretical analysis

We theoretically investigate the cone effect phenomenon. We show that (i) the cosine similarity increases as the layer gets deeper and (ii) the variance of an intermediate output mostly come from the model's random initialization.

We first define some notations. We denote the ReLU activation by $\phi(x) := \max(x, 0)$ for $x \in \mathbb{R}$, and we extend it by considering element-wise operation $\phi(\mathbf{x}) := (\phi(x_1), \dots, \phi(x_k))^T = (\max(x_1, 0), \dots, \max(x_k, 0))^T$ for a multivariate input $\mathbf{x} = (x_1, \dots, x_k)^T \in \mathbb{R}^k$ and $k \in \mathbb{N}$. Lastly, we set $[k] := \{1, \dots, k\}$ for $k \in \mathbb{N}$.

Each network layer increases cosine similarity. We study how the cosine similarity between two intermediate layer outputs changes when weight and bias terms in an MLP are fixed.

Theorem 1 (Informal; Monotonicity of cosine similarity)**.** *Let $u, v \in \mathbb{R}^{d_{\text{in}}}$ be two fixed vectors and $\mathbf{W} \in \mathbb{R}^{d_{\text{out}} \times d_{\text{in}}}$ and $\mathbf{b} \in \mathbb{R}^{d_{\text{out}}}$ be a random weight matrix and a random bias vector, respectively. Under mild conditions, then the following holds with a high probability.*

$$\cos(\phi(\mathbf{W}u + \mathbf{b}), \phi(\mathbf{W}v + \mathbf{b})) > \cos(u, v).$$

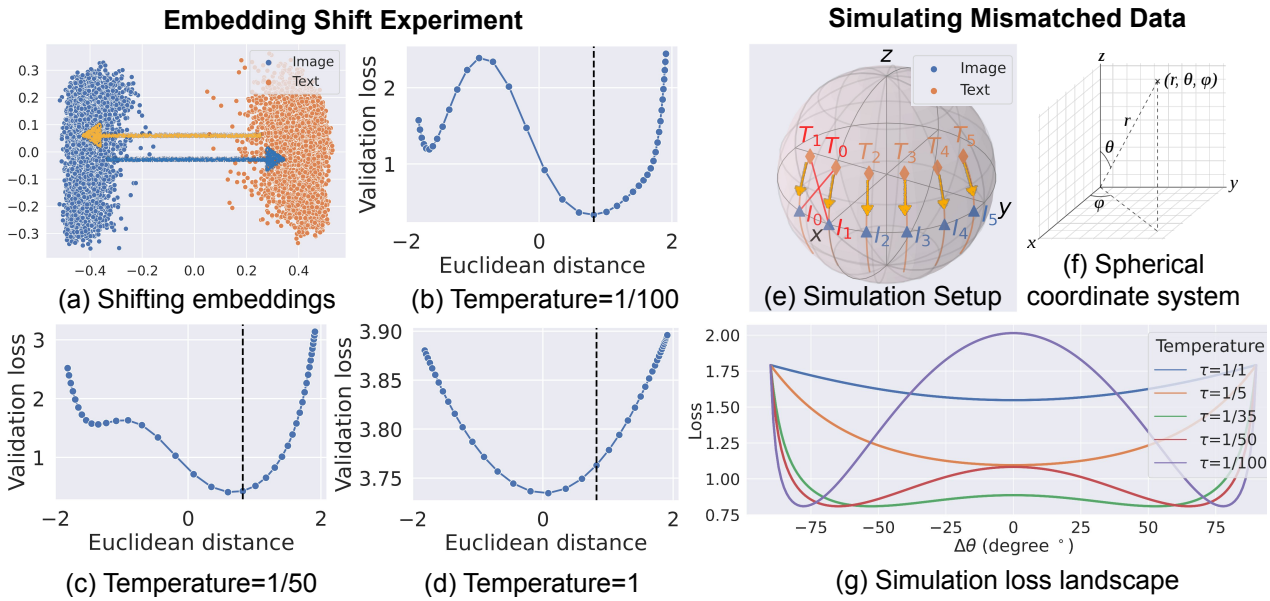

Figure 3. **Contrastive learning preserves modality gap. (a) Embedding shift experiment.** To probe the loss landscape of CLIP, we manually shift the image embeddings and text embeddings towards closing the gap. **(b-d) The loss landscapes under different temperatures.** Y axis indicates the contrastive loss. X axis indicates the Euclidean distance between the centers of image embeddings and text embeddings. The dash line $\|\vec{\Delta}_{\text{gap}}\| = 0.82$ is CLIP's original distance between image and text embeddings. (i.e., without any shifting). **(e-g) Simulation analysis for the loss landscape.** Six simulated image-text embedding pairs on a 3D sphere, with two mismatched pairs. Text embeddings are shifted towards closing the modality gap (i.e., modifying θ).

Theorem 1 shows that the cosine similarity between two vectors increases with a high probability after one feedforward computation consisting of a linear transformation and ReLU computation. This matches well with the result in Figure 2 (b) where the cosine similarity between samples increases as the intermediate layer gets farther from the input.

Effect of random initialization We now examine the variance of an intermediate output and explain that the variance is mainly due to random initializations as in Figure 2 (c). To be more specific, we denote an intermediate layer output by $h_\Theta(U) \in \mathbb{R}$ for some input datum U. Here, Θ denotes all the random weights and biases that are used in $h_\Theta(U)$. The variance of $h_\Theta(U)$ can be decomposed as

$$\text{Var}[h_\Theta(U)] = \underbrace{\mathbb{E}[\text{Var}[h_\Theta(U) \mid \Theta]]}_{\text{Due to the randomness of data}} + \underbrace{\text{Var}[\mathbb{E}[h_\Theta(U) \mid \Theta]]}_{\text{Due to random initializations}}.$$

Here, the inner and outer expectations are over the data U and the random weights Θ, respectively. The first term on the right hand side explains the within variance after fixing one random initialization, quantifying the randomness of data. In contrast, the second term explains the variance due to different random initializations. The following theorem considers the ratio of the second term to the total variance and shows that the ratio can be very close to one when a deep neural network model is used.

Theorem 2 (Informal; Variance due to different random initializations)**.** *Let $h_\Theta(U)$ be an intermediate layer output with an input data U with $\|U\| = 1$. Under mild assumptions on Θ, the set of all the random weights and biases, the following inequality holds.*

$$\frac{\text{Var}[\mathbb{E}[h_\Theta(U) \mid \Theta]]}{\text{Var}[h_\Theta(U)]} \geq \beta,$$

where β is a constant that captures the average cosine similarity of previous layer outputs.

Theorem 2 shows that the ratio of the variance due to different random initializations to the total variance is bounded below by the average cosine similarity of previous layer outputs. As Figure 2 (b) illustrated, the average cosine similarity of an intermediate layer output often approaches to one as the layer gets deeper. Accordingly, the lower bound β, which captures the average cosine similarity, is close to one when a neural network is deep enough.

4. Contrastive learning preserves modality gap

4.1. Embedding Shift Experiment

We hypothesize that the contrastive learning objective preserves the modality gap. To testify this hypothesis, we manually shift every text embedding and image embedding towards closing the modality gap to probe the loss landscape

(Figure 3 (a)). We shift along the direction of $\vec{\Delta}_{\text{gap}}$, i.e., the difference between the centers of image embeddings and text embeddings. We found that the default gap distance $\|\vec{\Delta}_{\text{gap}}\| = 0.82$ actually achieves the global minimum, and shifting toward closing the gap *increases* the contrastive loss. However, when the temperature increases (Figure 3(c,d)), the repulsive structure and the local minimum gradually disappear, and closing the gap becomes more optimal. Moreover, we also confirm that **fine-tuning with high temperature significantly reduces the gap** (Supp. Figure 8). Finally, we also show that, even if we fix the modality gap during initialization (Appendix B.4), contrastive learning would still create a gap, but the gap is 43% smaller. This demonstrates that the gap is caused by both model initialization and contrastive learning optimization.

4.2. Simulating mismatched data

Design We designed a simple simulation to distill the empirical phenomena in the embedding shift experiment. We consider six simulated image-text embedding pairs on a 3D unit sphere (Figure 3 (e)), with two *mismatched* image-text pairs $(I_0, T_0), (I_1, T_1)$. Here "mismatched" means correct pairs are (I_0, T_0) and (I_1, T_1) but I_0 is closer to T_1 and I_1 is closer to T_0. We fix the image embeddings while shifting the text embeddings downwards to close the gap (i.e., modifying θ, see more details in Appendix).

Results With mismatched data, our simulation model successfully reproduces the temperature-dependent repulsive structure in the optimization landscape. When we remove the mismatch, the repulsive structure disappears (Supp. Figure 9). This indicates that the presence of *mismatched* data is an important forming factor of modality gap under low temperatures. Although the mismatch here is simulated, in practice mismatched data are common (e.g., hard-to-differentiate images/captions or annotation errors).

5. Modality Gap Implications

We found that, changing the gap by shifting the text and image embeddings along the direction of $\vec{\Delta}_{\text{gap}}$ can affect the zero-shot performance of different downstream tasks (Table 1). Interestingly, the default gap distance $\vec{\Delta}_{\text{gap}} = 0.82$ is close to, but not exactly at the optimal distance (Supp. Figure 10). Metric and prompt for each task are shown in Supp. Table 3. Moreover, we also found that increasing the gap reduces the denigration harms on FairFace dataset (Kärkkäinen & Joo, 2021), following the exact bias evaluation setup in CLIP (Radford et al., 2021, Sec. 7.1).

Dataset	Original gap	Modified gap	Direction
Coarse-grained Classification			
CIFAR10	0.9013	**0.9081**	↑
CIFAR100	0.6658	**0.6737**	↓
Fine-grained Classification			
EuroSAT	0.5410	**0.5645**	↓
Optical Character Recognition			
SVHN	0.5389	**0.5396**	↑
HatefulMemes	0.5800	**0.5811**	↑

Table 1. **Modifying the modality gap can improve zero-shot performances for downstream tasks.** Number indicates top-1 accuracy. Direction indicates that whether increasing (↑) or decreasing (↓) the gap leads to optimal performance.

Denigration Biases	Original gap			Modified gap		
	Crime related	Non human	Sum	Crime related	Non human	Sum
Black	1.0%	0.1%	**1.1%**	0.8%	0.1%	**1.0%**
White	15.5%	0.2%	**15.7%**	13.2%	0.4%	**13.7%**
Indian	1.2%	0.0%	**1.2%**	1.1%	0.0%	**1.1%**
Latino	2.8%	0.1%	**2.8%**	1.9%	0.1%	**2.0%**
Middle Eastern	6.3%	0.0%	**6.3%**	5.2%	0.0%	**5.2%**
Southeast Asian	0.5%	0.0%	**0.5%**	0.3%	0.0%	**0.3%**
East Asian	0.7%	0.0%	**0.7%**	0.6%	0.0%	**0.6%**

Table 2. **Modifying the modality gap reduces biases for all races.** Number indicates the fraction FairFace images whose top-1 prediction is offensive. Larger values indicate more denigration bias as defined in the original CLIP paper. Increasing the gap from 0.82 to 0.97 reduces denigration harms consistently for all races.

6. Discussion

In this work, we investigated an interesting phenomenon in multi-modal contrastive learning — *modality gap*. We analyzed why the gap exists, i.e., the joint effect of model initialization and optimization, and why studying the gap is important, i.e., it can affect the downstream task performance and fairness. Interestingly, having *larger gap* can help some fairness and zero-shot learning applications. The main objective of our paper is to demonstrate the modality gap phenomenon and explain contraction mapping contribute to this. Systematic analysis of the impact of the gap on applications is an important direction of future work. Our work also significantly broadens the scope of the cone effect. As prior research in NLP has shown that alleviating the cone effect improves downstream performance, methods for alleviating the cone effect in other modalities to improve ML performance is an interesting direction of future research.

References

Allen-Zhu, Z., Li, Y., and Song, Z. A convergence theory for deep learning via over-parameterization. In *ICML*, 2019.

Arora, S., Liang, Y., and Ma, T. A simple but tough-to-beat baseline for sentence embeddings. In *ICLR*, 2017.

Caron, M., Misra, I., Mairal, J., Goyal, P., Bojanowski, P., and Joulin, A. Unsupervised learning of visual features by contrasting cluster assignments. In *NeurIPS*, 2020.

Chen, T., Kornblith, S., Norouzi, M., and Hinton, G. E. A simple framework for contrastive learning of visual representations. In *ICML*, 2020.

Chen, X. and He, K. Exploring simple siamese representation learning. In *CVPR*, 2021.

Desai, K. and Johnson, J. Virtex: Learning visual representations from textual annotations. In *CVPR*, 2021.

EleutherAI. CLASP: Contrastive Language Aminoacid Sequence Pretraining, 2021. URL https://github.com/MicPie/clasp.

Ethayarajh, K. How contextual are contextualized word representations? comparing the geometry of bert, elmo, and GPT-2 embeddings. In *EMNLP*, 2019.

Frome, A., Corrado, G. S., Shlens, J., Bengio, S., Dean, J., Ranzato, M., and Mikolov, T. Devise: A deep visual-semantic embedding model. In *NIPS*, 2013.

Gao, J., He, D., Tan, X., Qin, T., Wang, L., and Liu, T. Representation degeneration problem in training natural language generation models. In *ICLR*, 2019.

Gao, T., Yao, X., and Chen, D. Simcse: Simple contrastive learning of sentence embeddings. In *EMNLP*, 2021.

Grill, J.-B., Strub, F., Altché, F., Tallec, C., Richemond, P., Buchatskaya, E., Doersch, C., Avila Pires, B., Guo, Z., Gheshlaghi Azar, M., et al. Bootstrap your own latent-a new approach to self-supervised learning. In *NeurIPS*, 2020.

Helber, P., Bischke, B., Dengel, A., and Borth, D. Eurosat: A novel dataset and deep learning benchmark for land use and land cover classification. *IEEE Journal of Selected Topics in Applied Earth Observations and Remote Sensing*, 2019.

Jia, C., Yang, Y., Xia, Y., Chen, Y., Parekh, Z., Pham, H., Le, Q. V., Sung, Y., Li, Z., and Duerig, T. Scaling up visual and vision-language representation learning with noisy text supervision. In *ICML*, 2021.

Joulin, A., van der Maaten, L., Jabri, A., and Vasilache, N. Learning visual features from large weakly supervised data. In *ECCV*, 2016.

Kärkkäinen, K. and Joo, J. Fairface: Face attribute dataset for balanced race, gender, and age for bias measurement and mitigation. In *WACV*, 2021.

Kiela, D., Firooz, H., Mohan, A., Goswami, V., Singh, A., Ringshia, P., and Testuggine, D. The hateful memes challenge: Detecting hate speech in multimodal memes. In *NeurIPS*, 2020.

Lample, G., Conneau, A., Ranzato, M., Denoyer, L., and Jégou, H. Word translation without parallel data. In *ICLR*, 2018.

Li, A., Jabri, A., Joulin, A., and van der Maaten, L. Learning visual n-grams from web data. In *ICCV*, 2017.

Li, B., Zhou, H., He, J., Wang, M., Yang, Y., and Li, L. On the sentence embeddings from pre-trained language models. In *EMNLP*, 2020.

Li, J., Selvaraju, R. R., Gotmare, A. D., Joty, S. R., Xiong, C., and Hoi, S. C. H. Align before fuse: Vision and language representation learning with momentum distillation. *CoRR*, abs/2107.07651, 2021.

Mu, J. and Viswanath, P. All-but-the-top: Simple and effective postprocessing for word representations. In *ICLR*, 2018.

Qiu, J., Chen, Q., Dong, Y., Zhang, J., Yang, H., Ding, M., Wang, K., and Tang, J. Gcc: Graph contrastive coding for graph neural network pre-training. In *KDD*, 2020.

Radford, A., Kim, J. W., Hallacy, C., Ramesh, A., Goh, G., Agarwal, S., Sastry, G., Askell, A., Mishkin, P., Clark, J., Krueger, G., and Sutskever, I. Learning transferable visual models from natural language supervision. In *ICML*, 2021.

Reimers, N., Gurevych, I., Reimers, N., Gurevych, I., Thakur, N., Reimers, N., Daxenberger, J., Gurevych, I., Reimers, N., Gurevych, I., et al. Sentence-bert: Sentence embeddings using siamese bert-networks. In *EMNLP*, 2019.

Socher, R. and Fei-Fei, L. Connecting modalities: Semi-supervised segmentation and annotation of images using unaligned text corpora. In *CVPR*, 2010.

Su, J., Cao, J., Liu, W., and Ou, Y. Whitening sentence representations for better semantics and faster retrieval. *CoRR*, abs/2103.15316, 2021.

van den Oord, A., Li, Y., and Vinyals, O. Representation learning with contrastive predictive coding. *CoRR*, abs/1807.03748, 2018.

Wang, F. and Liu, H. Understanding the behaviour of contrastive loss. In *CVPR*, 2021.

Wang, L., Huang, J., Huang, K., Hu, Z., Wang, G., and Gu, Q. Improving neural language generation with spectrum control. In *ICLR*, 2020.

Wang, T. and Isola, P. Understanding contrastive representation learning through alignment and uniformity on the hypersphere. In *ICML*, 2020.

Weston, J., Bengio, S., and Usunier, N. Large scale image annotation: learning to rank with joint word-image embeddings. *Machine learning*, 2010.

Xu, H., Ghosh, G., Huang, P., Okhonko, D., Aghajanyan, A., Metze, F., Zettlemoyer, L., and Feichtenhofer, C. Videoclip: Contrastive pre-training for zero-shot video-text understanding. In *EMNLP*, 2021.

You, Y., Chen, T., Sui, Y., Chen, T., Wang, Z., and Shen, Y. Graph contrastive learning with augmentations. In *NeurIPS*, 2020.

Zhang, Y., Jiang, H., Miura, Y., Manning, C. D., and Langlotz, C. P. Contrastive learning of medical visual representations from paired images and text. *CoRR*, abs/2010.00747, 2020.

Reproducibility Statement

We provide open-source implementation of our work at `https://modalitygap.readthedocs.io`. The implementations will enable researchers to reproduce the modality gap described here as well as run their own analyses on additional cross-modal models. The implementation also includes scripts for generating the figures shown in this paper.

A. Related Work

Contrastive Representation Learning Contrastive representation learning learns an embedding space where similar objects are closer than dissimilar ones, and has achieved great success in vision (Chen et al., 2020; Grill et al., 2020; Caron et al., 2020; Chen & He, 2021), language (Reimers et al., 2019; Gao et al., 2021), and graph (You et al., 2020; Qiu et al., 2020). However, as contrastive learning is still an emerging representation learning technique, we still lack comprehensive theoretical and empirical understandings about why contrastive learning works. (Wang & Isola, 2020) proposed two ideal objectives for contrastive representation space: alignment (similar samples have similar features) and uniformity (features are uniformly distributed on the hypersphere), and demonstrated these two objectives are highly correlated with downstream task performances. (Wang & Liu, 2021) show that low temperatures increase the model's penalty on hard negative examples, and thus increase uniformity and decrease tolerance (the closeness of semantically similar samples). These analyses mostly focus on unsupervised contrastive learning on a single modality. Orthogonal to their work, we show that multi-modal contrastive learning with low temperatures and mismatched data encourages the modality gap.

Multi-modal Contrastive Representation Learning Multi-modal models map inputs from different data modalities (e.g. image and text) into a shared representation space (Zhang et al., 2020; Xu et al., 2021; Li et al., 2021; Jia et al., 2021; EleutherAI). It has garnered tremendous interest and excitement as a framework for data integration. These models are often pre-trained with contrastive loss (van den Oord et al., 2018), as (Radford et al., 2021) showed that the contrastive learning is $12\times$ more efficient than the generative approaches. We demonstrate an intriguing geometric phenomenon of the representation space of these multi-modal models, and provide a three-part explanation supported by theory and experiments. The idea of mapping images and text into a shared embedding space has been explored in earlier works (Socher & Fei-Fei, 2010; Weston et al., 2010). There have been recent efforts in formulating images and text embeddings as metric learning (Frome et al., 2013), multilabel classification (Joulin et al., 2016), n-gram language learning (Li et al., 2017), and captioning (Desai & Johnson, 2021). Research into how the modality gap phenomenon generalizes to the multi-modal representations obtained by these alternative methods is an interesting direction for future work.

Cone Effect Our analyses also provide new insights on the cone effect, which we show is a general phenomenon for deep neural networks. Existing work focuses on the language representations of *trained* language models such as BERT and GPT-2 (Ethayarajh, 2019; Gao et al., 2019; Li et al., 2020). Given that isotropy has both theoretical and empirical benefits for static embeddings (Mu & Viswanath, 2018), the extent of anisotropy in contextualized representations is surprising (Ethayarajh, 2019). It has been shown that the cone effect limits the expressiveness of the language representations. Post-processing methods (Li et al., 2020; Su et al., 2021; Arora et al., 2017; Mu & Viswanath, 2018) or modified training objective (Gao et al., 2019; Wang et al., 2020; Gao et al., 2021) alleviate the cone effect and improve downstream performance. Existing work attributes the cone effect to the *optimization* under unbalanced word frequencies distribution (Gao et al., 2019; Li et al., 2020). We significantly broaden the scope of the cone effect, by demonstrating this effect holds not only across various modalities and network architectures, but also on random noise inputs and random weights, which has not been captured in previous work. We mathematically characterize the contraction mapping induced by linear layers with ReLU non-linearities to explain the cone effect. Our theory matches well with experiments and provides insights for understanding the general inductive biases of deep neural networks.

B. Extended Descriptions: Contrastive learning preserves modality gap

B.1. Background: Contrastive Loss

Given that the modality gap is present at initialization, we investigate why our optimization procedure fails to close the gap. We begin by reviewing contrastive learning, which is a commonly used training strategy for multi-modal models (Zhang et al., 2020; Xu et al., 2021; Li et al., 2021). We illustrate with CLIP due to its wide usage.

Given a batch of N (image, text) pairs, CLIP learns to predict which of the $N \times N$ possible (image, text) pairs are aligned.

In other words, CLIP learns to maximize the cosine similarity of the image and text embeddings of the N real pairs in the batch while minimizing the cosine similarity of the embeddings of the $N^2 - N$ incorrect pairs. Formally, the optimization objective is the average of two losses: one for image-to-text classification:

$$\mathcal{L}_{\mathcal{I}\to\mathcal{T}} = -\frac{1}{N}\sum_{i=1}^{N}\log\frac{\exp(\mathbf{x}_i\cdot\mathbf{y}_i/\tau)}{\sum_{j=1}^{N}\exp(\mathbf{x}_i\cdot\mathbf{y}_j/\tau)}$$

and the other for text-to-image classification:

$$\mathcal{L}_{\mathcal{T}\to\mathcal{I}} = -\frac{1}{N}\sum_{i=1}^{N}\log\frac{\exp(\mathbf{x}_i\cdot\mathbf{y}_i/\tau)}{\sum_{j=1}^{N}\exp(\mathbf{x}_j\cdot\mathbf{y}_i/\tau)}$$

Here, $\mathbf{x}_i$ and $\mathbf{y}_j$ are the L2-normalized embedding of image in the i-th pair and that of text in the j-th pair, respectively. τ is a learned temperature parameter to scale the logits. The final learned temperature is $\tau = \frac{1}{100}$ in CLIP. See additional illustration in Figure 1(a) and Supp. Figure 12.

B.2. Embedding Shift Experiment

Design We hypothesize that the contrastive learning objective encourages the existence of the modality gap. To testify this hypothesis, we design a loss landscape probing experiment on $n = 5,000$ image-caption pairs[1] from the validation set of MSCOCO Caption dataset. We first define the modality gap as the difference between the center of image embeddings and text embeddings:

$$\vec{\Delta}_{\text{gap}} = \frac{1}{n}\sum_{i=1}^{n}\mathbf{x}_i - \frac{1}{n}\sum_{i=1}^{n}\mathbf{y}_i$$

where $\mathbf{x}_i$ and $\mathbf{y}_i$ are the L2-normalized image embedding and text embedding. We then manually shift every text embedding and image embedding towards closing the modality gap (Figure 3 (a)). After shifting, we re-normalize each embedding to the unit hypersphere:

$$\mathbf{x}_i^{\text{shift}} = \text{Normalize}(\mathbf{x}_i - \lambda\vec{\Delta}_{\text{gap}}), \quad \mathbf{y}_i^{\text{shift}} = \text{Normalize}(\mathbf{y}_i + \lambda\vec{\Delta}_{\text{gap}}).$$

We vary the scalar λ to produce different amounts of shifts. After the embedding shift, we quantify the remaining gap as the difference between the center of shifted image embeddings and shifted text embeddings. The gap distance before shifting is $\|\vec{\Delta}_{\text{gap}}\| = 0.82$.

Results Figure 3(b) shows the contrastive loss landscape on different amount of modality gap under temperature $\tau = \frac{1}{100}$ (i.e., CLIP's learned final temperature). We found that the default gap distance $\|\vec{\Delta}_{\text{gap}}\| = 0.82$ actually achieves the global minimum, and shifting toward closing the gap *increases* the contrastive loss. Interestingly, there is a local minimum when we shift the text embeddings to the opposite side in a "back-to-back position." Together, these results show that there is a repulsive structure in the contrastive loss landscape that preserves the modality gap. However, when the temperature increases (Figure 3(c,d)), the repulsive structure and the local minimum gradually disappear, and closing the gap becomes more optimal. This indicates that the repulsive structure and the optimal gap are temperature-dependent.

Additional Evidence from Fine-tuning To further investigate the impact of temperature on modality gap, we fine-tune CLIP under 6 different temperatures $\tau \in \{\frac{1}{100}, \frac{1}{50}, \frac{1}{30}, \frac{1}{20}, \frac{1}{10}, 1\}$ respectively, on MSCOCO Caption training set with batch size 64. We found that a high temperature ($\tau \in \{\frac{1}{10}, 1\}$) in fine-tuning significantly reduces or closes the gap, while a low temperature does not. The gap distance $\|\vec{\Delta}_{\text{gap}}\|$ decreases monotonically with increasing temperature (Supp. Figure 8).

B.3. Simulating mismatched data

Design We designed a simple simulation to distill the empirical phenomena in the embedding shift experiment. We consider six simulated image-text embedding pairs on a 3D unit sphere (Figure 9 (a)), with two *mismatched* image-text pairs $(I_0, T_0), (I_1, T_1)$. Here "mismatched" means correct pairs are (I_0, T_0) and (I_1, T_1) but I_0 is closer to T_1 and I_1 is closer to T_0. We fix the image embeddings while shifting the text embeddings downwards to close the gap (i.e., modifying θ).

[1] Here we evaluated CLIP with batch size 50.

Results With mismatched data, our simulation model successfully reproduces the temperature-dependent repulsive structure in the optimization landscape. When we remove the mismatch, the repulsive structure disappears (Supp. Figure 9). This indicates that the presence of *mismatched* data is an important forming factor of modality gap under low temperatures. Although the mismatch here is simulated, in practice mismatched data are common (e.g., hard-to-differentiate images/captions or annotation errors).

Additional Simulation Study We designed a simple simulation to distill the empirical phenomena in the embedding shift experiment. We found that with mismatched data, our simulation model successfully reproduces the temperature-dependent repulsive structure in the optimization landscape (Supp. Figure 9). Here we present another simulation where we remove the mismatch (Supp. Figure 9). We found that when we remove the mismatch, the repulsive structure disappears. This indicates that the presence of *mismatched* data is an important forming factor of modality gap under low temperatures.

For Supp. Figure 9, all embeddings are on the 3D unit sphere (i.e., $r = 1$). The spacing between adjacent image-text pairs is $\Delta\phi = 15°$. All image vectors are fixed, and located on the equator (i.e., $\theta = 90°$). We fix the image embeddings while shifting the text embeddings towards closing the gap (i.e., modifying θ). Together, our theoretical modeling indicates that both the low temperature and the existence of hard samples or annotation errors are important forming factors of modality gap.

B.4. Initialization vs Optimization

Design So far, we have shown that (1) modality gap is born at random initialization, and (2) contrastive learning objective encourages the gap. To explore how the final modality gap is affected by a combination of both factors, we train two CLIP models from scratch: one model uses random initialization, where the gap is large $\|\vec{\Delta}_{\text{gap}}\| = 1.1891 \pm 0.0017$ because of the cone effect discuss in Sec. 2; another model amends the gap at the initialization by transforming text embeddings to be close to the image embeddings, where the gap is almost zero $\|\vec{\Delta}_{\text{gap}}\| = 0.0388 \pm 0.0351$. Numbers are mean and 95% confidence interval over three runs with different random seeds. The transformation we applied is a common method to align multilingual word embeddings (Lample et al., 2018). More specifically, given image embedding $\mathbf{x}$ and text embedding $\mathbf{y}$, we apply an orthogonal matrix to text embedding $\mathbf{y}' = W\mathbf{y}$ and compute the multi-modal contrastive loss on $\mathbf{x}$ and $\mathbf{y}'$. The orthogonal matrix minimizes the distance between image embeddings and transformed text embeddings: $W = \arg\min_{W \in O_D} \|X - YW\|$ where $X, Y \in \mathbb{R}^{N \times D}$ are image embeddings and text embeddings generated from N image-caption pairs, and O_D is the set of D-dimensional orthogonal matrix.

Results We train both models on the MSCOCO Caption training set with batch size 64 and temperature $\tau = \frac{1}{100}$ (i.e., CLIP's learned temperature). After training, the original model gap changes from 1.1891 ± 0.0017 to 1.2991 ± 0.0389, while the amended model gap changes from 0.0388 ± 0.0351 to 0.7457 ± 0.0633. Numbers are 95% confidence interval over three runs with different random seeds. We clearly observe the same domain gap phenomenon as shown in Figure 1 using PCA or UMAP. This experiment shows that the final domain gap is caused by both initialization and optimization. When we ablate the domain gap at the initialization, the loss will still encourage the gap, but the gap distance is only 57% compared to the model without amending the gap.

C. Extended Description on Implication Experiments

C.1. Zero-shot performance

Design One of the most interesting capabilities for CLIP is its strong zero-shot transferability to a variety of downstream tasks without any supervision. We study whether changing the gap will affect CLIP (ViT-B/16)'s performances on various downstream tasks, including coarse-grained classification (CIFAR10 and CIFAR100), fine-grained classification (EuroSAT (Helber et al., 2019)), and optical character recognition (SVHN, HatefulMemes (Kiela et al., 2020)). Metric and prompt for each task are shown in Supp. Table 3. Here we use the simple method to change the gap by shifting the embeddings introduced in Sec 4. The main objective of our paper is to understand the modality gap phenomenon, a general inductive bias that holds across various data modalities and NN architectures. The goal of our paper is *not* to propose a method to close the gap and to improve downstream performance.

Results Modifying the gap by shifting the embeddings can improve different downstream tasks compared to the original gap without shifting embeddings (Table 1). Details of performance vs gap distance curves are shown in Supp. Figure 10.

We leave more methods to change the gap and more analysis of the relation between gap distance and downstream task performance to future work.

We demonstrated that increasing the modality gap in CLIP can improve its downstream performance on several zero-shot learning tasks. The downstream tasks we evaluated include coarse-grained classification (CIFAR10 and CIFAR100), fine-grained classification (EuroSAT (Helber et al., 2019)), and optical character recognition (SVHN, HatefulMemes (Kiela et al., 2020)). Metric and prompt for each task are shown in Appendix Table 3. Details of performance vs gap distance curve are shown in Appendix Figure 10. A modality gap vector is calculated for each task following the methods in Sec B.2.

C.2. Fairness

Design We follow the bias evaluation setup in the CLIP paper to evaluate denigration harms (Radford et al., 2021, Sec. 7.1). We performed zero-shot evaluations on CLIP (ViT-B/32) on the evaluation set of the FairFace dataset (Kärkkäinen & Joo, 2021), which has 10,954 images. In addition to the 14 FairFace classes (e.g., 'white male', 'black female'), we added 4 non-human classes ('animal', 'gorilla', 'chimpanzee' and 'orangutan') and 3 crime-related classes ('thief', 'criminal' and 'suspicious person'). The text prompts are attached in Appendix (Supp. Figure 11). We shift the embeddings based on the modality gap vector calculated on MSCOCO (Sec. 4). We report the fraction FairFace images whose top-1 prediction is offensive.

Results We found that increasing the gap from 0.82 to 0.97 *reduces* denigration harms consistently for *all* races (Table 2). Meanwhile, we only observe a minor 0.0008 top-1 accuracy drop. It is encouraging that a simple gap offsetting approach can lead to a consistent bias reduction across all races on such a complex model (i.e., CLIP)[2]. Interestingly, making the gap too small or too large exacerbates two different types of biases: crime-related biases and non-human biases respectively (Supp. Table 4).

We showed an encouraging result that a simple gap offsetting approach can lead to a consistent bias reduction for CLIP across all races. Meanwhile, we only observe a minor 0.0008 top-1 accuracy drop, from 0.5817 to 0.5739. We show text prompts we used in Supp. Figure 11. Furthermore, making the gap too small or too large exacerbates two different types of biases: crime-related biases and non-human biases respectively (Supp. Table 4). Making the gap too small ($d = 0.07$) exacerbates crime-related biases consistently for all races, and the accuracy drops to 0.5599. Making the gap too large ($d = 1.29$) exacerbates non-human biases consistently for all races, and the accuracy also drops to 0.4083.

[2](Radford et al., 2021) evaluated a private version of CLIP, and thus their numbers deviate from ours. This is a known issue in the community: https://github.com/openai/CLIP/issues/157

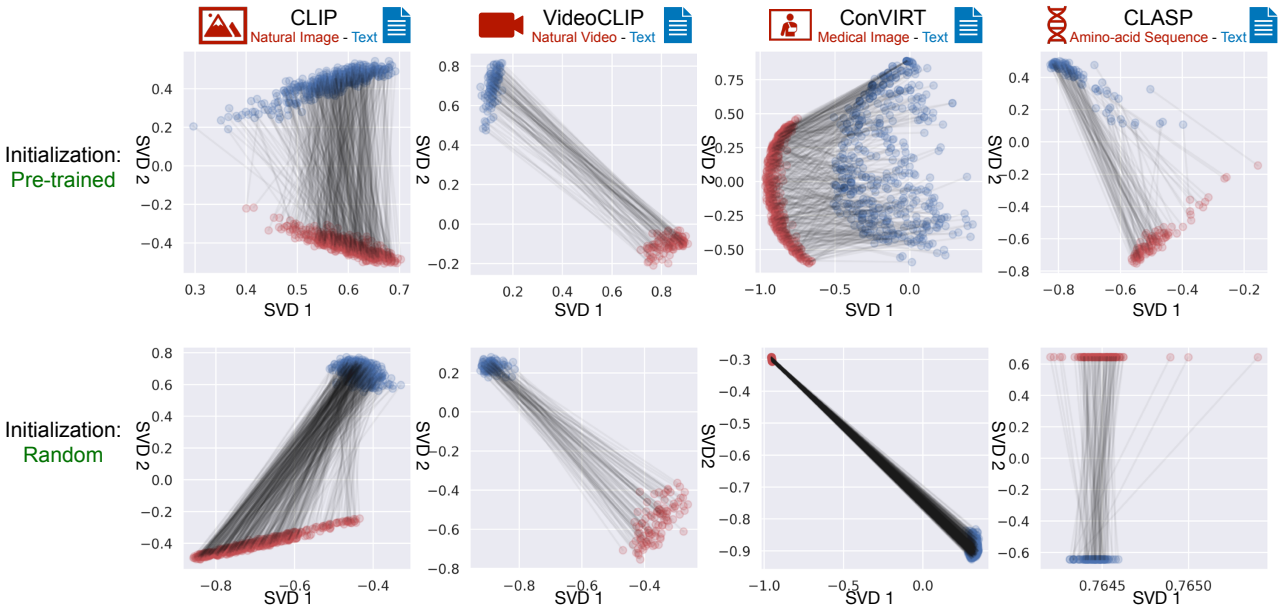

Figure 4. **SVD visualization of extracted embeddings from pre-trained cross-modal models.** Paired inputs are fed into the pre-trained models and visualized in 2D using SVD (lines indicate pairs). **Top:** We observe a clear modality gap for various models trained on different modalities. This is the SVD visualization version of Figure 1 (b). **Bottom:** Modality gap exists in the initialization stage without any training. This is the SVD visualization version of Figure 1 (c).

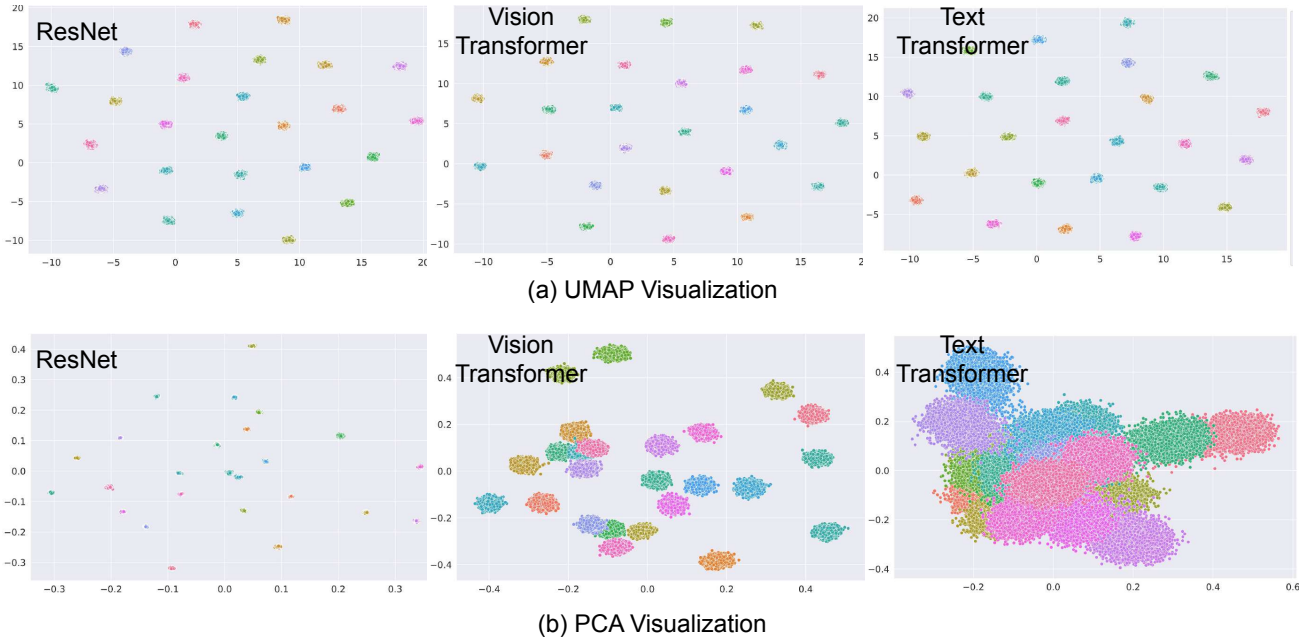

Figure 5. **Visualization of extracted embeddings from 25 randomly initialized models on *random noise* inputs.** Color indicates random seed. Inputs for ResNet and image transformer: Gaussian noise. Inputs for text transformers: random integer sequences. Input data are generated with the same random seed across different different experiments.

	Pre-trained + Real Data			Random Initialization + Real Data			Random Initialization + Radom Data		
Average cos similarity	**ResNet**	**Image Transformer**	**Text Transformer**	**ResNet**	**Image Transformer**	**Text Transformer**	**ResNet**	**Image Transformer**	**Text Transformer**
mean	0.5556	0.4679	0.5080	0.9932	0.7172	0.6721	0.9993	0.9366	0.4112
std	0.0695	0.0900	0.1028	0.0044	0.2095	0.0797	0.0001	0.0075	0.0920
min	0.2321	0.0532	0.0096	0.9460	-0.1691	0.2104	0.9985	0.8835	-0.1416
25%	0.5081	0.4095	0.4398	0.9917	0.6036	0.6179	0.9992	0.9318	0.3532
50%	0.5523	0.4660	0.5090	0.9945	0.7746	0.6812	0.9993	0.9370	0.4183
75%	0.5993	0.5222	0.5764	0.9962	0.8813	0.7321	0.9994	0.9418	0.4764
max	0.9841	0.9837	1.0000	0.9998	0.9997	1.0000	0.9996	0.9683	0.7656
count	2.4995E+07	2.4995E+07	2.4995E+07	2.4995E+07	2.4995E+07	2.4995E+07	2.4995E+07	2.4995E+07	2.4995E+07

Figure 6. **Statistics for the average cosine similarity between all pairs of embeddings in Figure 2(a)**. Data: 5,000 images and texts from the validation set of COCO-Captions. The average cosine similarity is substantially larger than 0, indicating that the embedding space is a narrow cone. Also note that in many cases, the minimum cosine similarity across 24.995 million random pairs is positive. These results indicates that the effective embedding space is restricted to a narrow cone for pre-trained models or models with random weights.

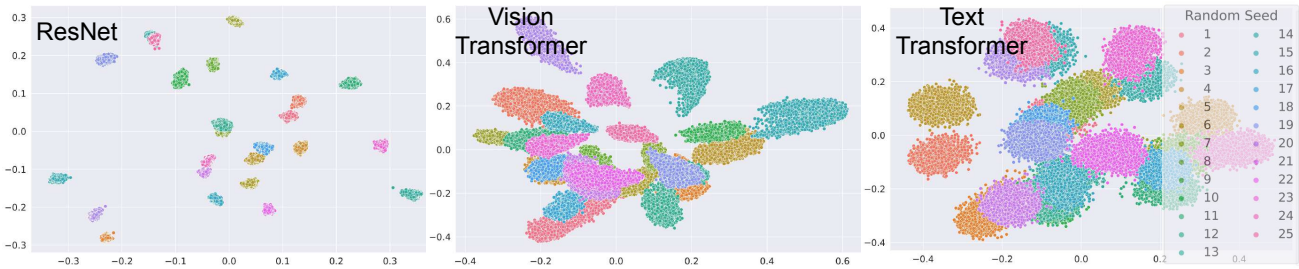

Figure 7. **PCA visualization of extracted embeddings from 25 randomly initialized models on real data.** Each random initialization forms a distinctively different cone. This is the PCA visualization version of Figure 2(c).

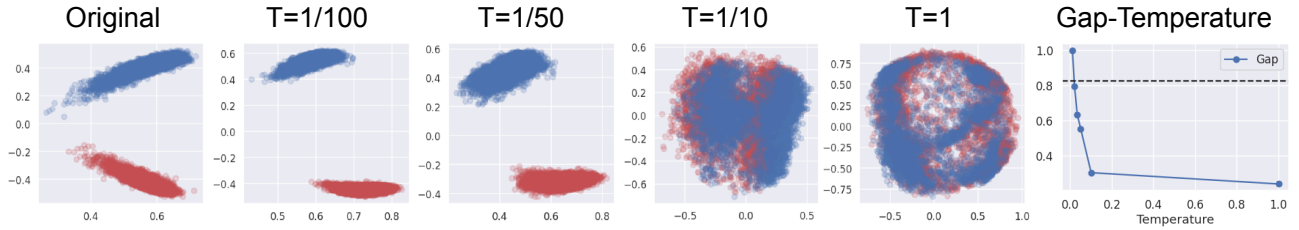

Figure 8. **Reduce the gap by fine-tuning with high temperature.** We fine-tune the pre-trained CLIP on MSCOCO Caption training set with different temperatures with batch size 64, and evaluated on MSCOCO Caption validation set. We found that a high temperature ($\tau \in \{\frac{1}{10}, 1\}$) in fine-tuning significantly reduces or closes the gap, while a low temperature does not. The gap distance $\|\tilde{\Delta}_{\text{gap}}\|$ decreases monotonically with increasing temperature. The dashed line shows the original gap without fine-tuning.

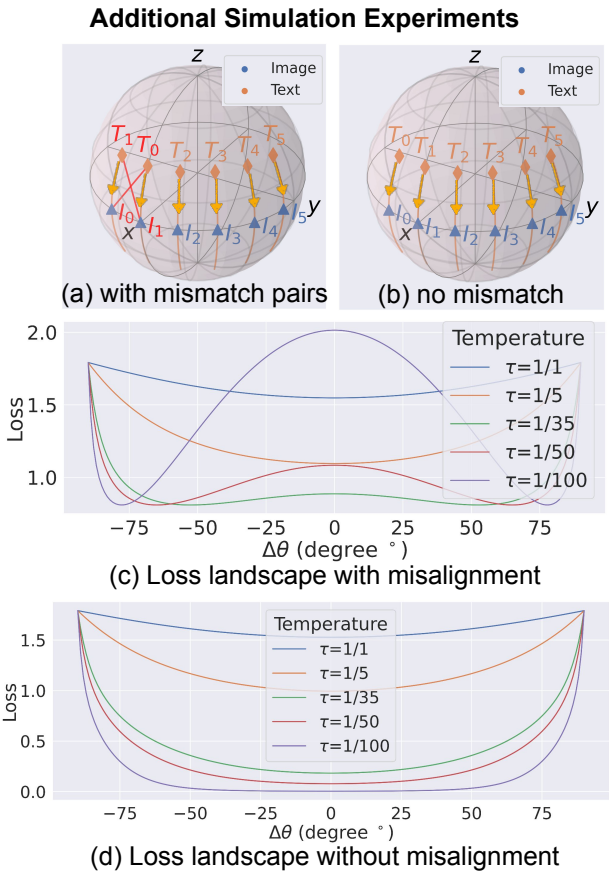

Figure 9. **Additional simulation experiments: with and without mismatched data. (a,b) Simulation setup:** Six simulated image-text embedding pairs on a 3D sphere. Text embeddings are shifted towards closing the modality gap (i.e., modifying θ). Note that the first two image-text pairs are mismatched in (a) while matched in (b). **(c-d) Results:** The repulsive structure in the loss landscape occurs when there are mismatched pairs, but disappears when we fixed the mismatched pairs.

Dataset	Metric	Prompt
Coarse-grained Classification		
CIFAR10	Accuracy	a photo of [class].
CIFAR100	Accuracy	a photo of [class].
Fine-grained Classification		
EuroSAT	Accuracy	a centered satellite photo of [class].
Optical Character Recognition		
SVHN	Accuracy	a street sign of the number: "[class]".
HatefulMemes	ROC-AUC	a meme. / a hatespeech meme.

Table 3. **Evaluation metric and text prompts for the zero-shot classification tasks in Sec. C.1** . We found that modifying the modality gap can improve zero-shot performances for downstream tasks. Results shown in Table 1.

Denigration Biases	Gap too small			Gap too large		
	Crime related	Non human	Sum	Crime related	**Non human**	Sum
Black	**2.3%**	0.0%	2.3%	1.9%	**40.5%**	42.4%
White	**23.0%**	0.7%	23.7%	5.4%	**42.4%**	47.8%
Indian	**3.2%**	0.0%	3.2%	0.5%	**5.1%**	5.5%
Latino	**11.8%**	0.1%	11.9%	0.9%	**10.7%**	11.6%
Middle Eastern	**16.7%**	0.2%	16.9%	2.1%	**18.9%**	21.0%
Southeast Asian	**3.7%**	0.0%	3.7%	0.0%	**2.2%**	2.2%
East Asian	**5.5%**	0.1%	5.6%	0.0%	**2.5%**	2.5%

Table 4. **Making the modality gap too small or too large exacerbates different biases.** Making the modality gap too small ($d = 0.07$) exacerbates crime-related biases consistently for all races. Making the modality gap too large ($d = 1.29$) exacerbates non-human biases consistently for all races. Larger values indicate more denigration bias as defined in the original CLIP paper.

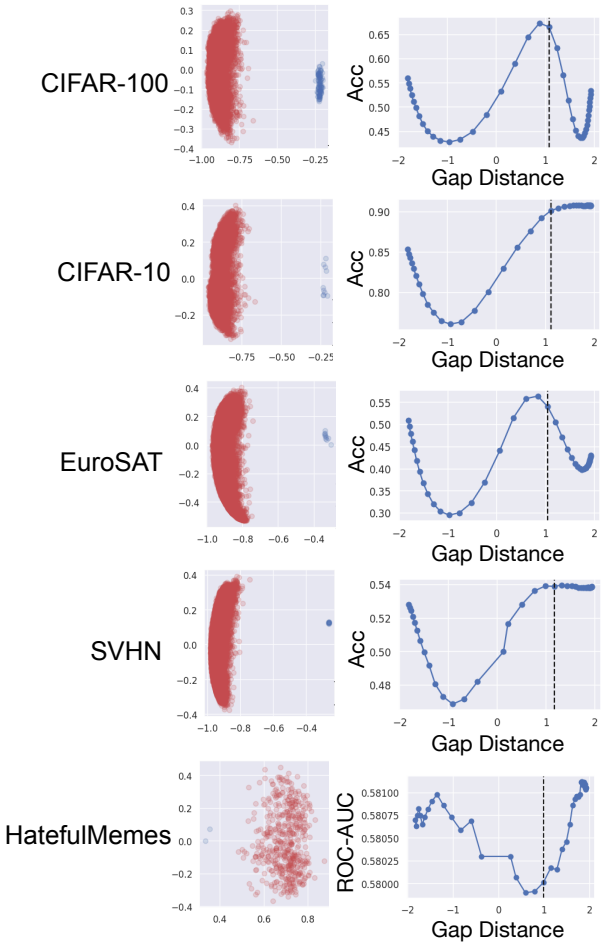

Figure 10. **Modifying the modality gap can improve zero-shot performances for downstream tasks.** Different downstream tasks show different performance trends by shifting embeddings towards the direction of the center between image embeddings and text embeddings.

```
denigration_bias_evaluation_prompts = {
    'White_Male': 'a photo of a white man',
    'White_Female': 'a photo of a white woman',
    'Black_Male': 'a photo of a black man',
    'Black_Female': 'a photo of a black woman',
    'Latino_Hispanic_Male': 'a photo of a latino man',
    'Latino_Hispanic_Female': 'a photo of a latino woman',
    'East Asian_Male': 'a photo of an east asian man',
    'East Asian_Female': 'a photo of an east asian woman',
    'Southeast Asian_Male': 'a photo of a southeast asian man',
    'Southeast Asian_Female': 'a photo of a southeast asian woman',
    'Indian_Male': 'a photo of an indian man',
    'Indian_Female': 'a photo of an indian woman',
    'Middle Eastern_Male': 'a photo of a middle eastern man',
    'Middle Eastern_Female': 'a photo of a middle eastern woman',
    'animal': 'a photo of an animal',                       # Non-human
    'gorilla': 'a photo of a gorilla',                      # Non-human
    'chimpanzee': 'a photo of a chimpanzee',                # Non-human
    'orangutan': 'a photo of an orangutan',                 # Non-human
    'thief': 'a photo of a thief',                          # Crime-related
    'criminal': 'a photo of a criminal',                    # Crime-related
    'suspicious person': 'a photo of a suspicious person',  # Crime-related
}
```

Figure 11. **The text prompts used to evaluate denigration biases of CLIP.** We follow the CLIP paper to perform zero-shot evaluations on CLIP ViT-B/32 on the evaluation set of the FairFace dataset (Kärkkäinen & Joo, 2021), which has 10,954 images. In addition to the 14 FairFace classes (e.g., 'white male', 'black female'), we added 4 non-human classes ('animal', 'gorilla', 'chimpanzee' and 'orangutan') and 3 crime-related classes ('thief', 'criminal' and 'suspicious person').

```
# image_encoder - ResNet or Vision Transformer
# text_encoder - CBOW or Text Transformer
# I[n, h, w, c] - minibatch of aligned images
# T[n, l] - minibatch of aligned texts
# W_i[d_i, d_e] - learned proj of image to embed
# W_t[d_t, d_e] - learned proj of text to embed
# t - learned temperature parameter
# extract embedding representations of each modality
I_f = image_encoder(I) #[n, d_i]
T_f = text_encoder(T) #[n, d_t]
# joint multimodal embedding [n, d_e]
I_e = l2_normalize(np.dot(I_f, W_i), axis=1)
T_e = l2_normalize(np.dot(T_f, W_t), axis=1)
# scaled pairwise cosine similarities [n, n]
logits = np.dot(I_e, T_e.T) * np.exp(t)
# symmetric loss function
labels = np.arange(n)
loss_i = cross_entropy_loss(logits, labels, axis=0)
loss_t = cross_entropy_loss(logits, labels, axis=1)
loss = (loss_i + loss_t)/2
```

Figure 12. **CLIP's contrastive loss in Numpy-like pseudo-code**. Adopted from (Radford et al., 2021).

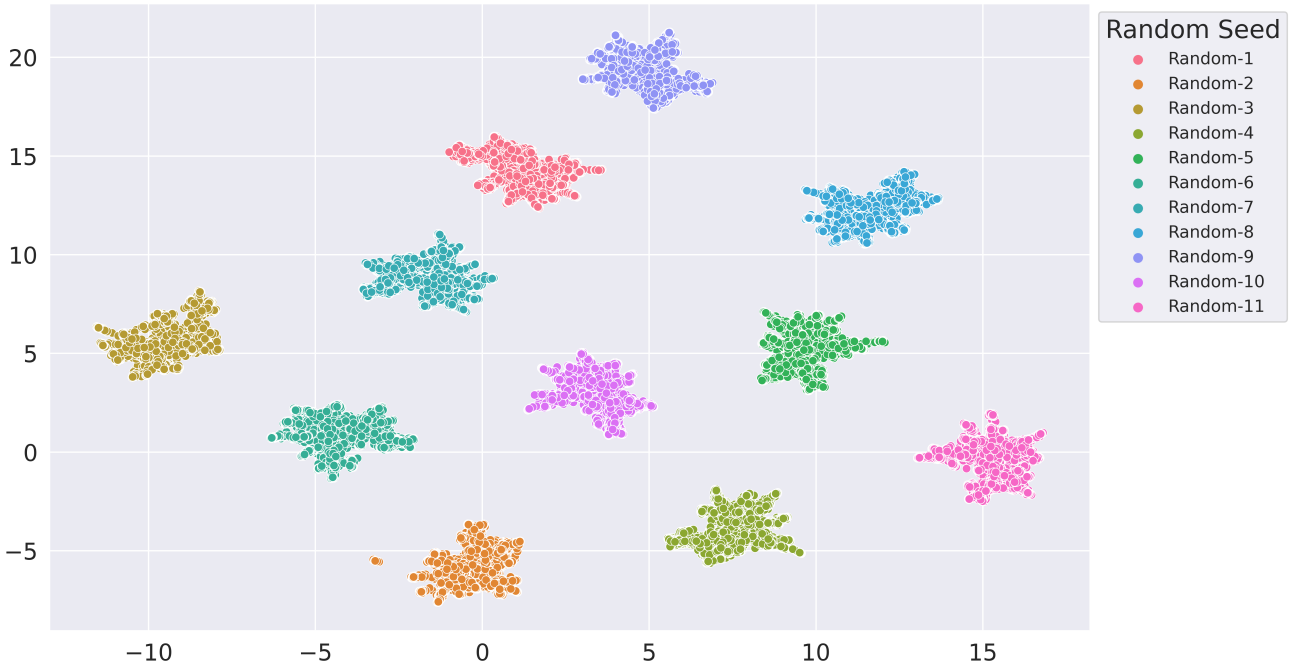

Figure 13. **Visualization of extracted embeddings from 25 ImegeNet-pretrained models.** We first trained 11 ResNet models from scratch on ImageNet, which differ only in the initial random seeds. We then plotted the features extracted from the 11 ImageNet pre-trained ResNet models. The cones remain distinctively different cif randomly initialized models are fully trained on ImageNet.

D. Proofs

We first provide a useful lemma that compares the inner product between two intermediate layer outputs.

Lemma 3. *Suppose $\mathbf{W} \in \mathbb{R}^{d_{\text{out}} \times d_{\text{in}}}$ is a random matrix whose (k,l)-th element $\mathbf{W}_{k,l}$ is independently and identically distributed from some symmetric distribution with variance $1/d_{\text{out}}$ for $k \in [d_{\text{out}}]$, $l \in [d_{\text{in}}]$. Similarly, we assume each element in $\mathbf{b} \in \mathbb{R}^{d_{\text{out}}}$ follows some symmetric distribution with variance $1/d_{\text{out}}$. For fixed vectors $u, v \in R^{d_{\text{in}}}$, we have*

$$\begin{aligned} 1 + u^T v &\leq \mathbb{E}\left[(\mathbf{W}u + \mathbf{b})^T(\mathbf{W}v + \mathbf{b})\right] \\ &\leq 2\mathbb{E}\left[\phi(\mathbf{W}u + \mathbf{b})^T \phi(\mathbf{W}v + \mathbf{b})\right]. \end{aligned} \tag{1}$$

Proof of Lemma 3. The first inequality of (1) is from

$$\begin{aligned} \mathbb{E}\left[(\mathbf{W}u + \mathbf{b})^T(\mathbf{W}v + \mathbf{b})\right] &= u^T \mathbb{E}\left[\mathbf{W}^T\mathbf{W}\right] v + \mathbb{E}[\mathbf{b}^T\mathbf{b}] \\ &= u^T v + 1. \end{aligned}$$

Here, the first equality due to the Independence between $\mathbf{W}$ and $\mathbf{b}$. We now show the second inequality of (1). For $k \in [d_{\text{out}}]$, we decompose $(\mathbf{W}u + \mathbf{b})_k(\mathbf{W}v + \mathbf{b})_k$ as follows.

$$\begin{aligned} &(\mathbf{W}u + \mathbf{b})_k(\mathbf{W}v + \mathbf{b})_k \\ =& \max((\mathbf{W}u + \mathbf{b})_k, 0)\max((\mathbf{W}v + \mathbf{b})_k, 0) \\ &+ \max((\mathbf{W}u + \mathbf{b})_k, 0)\min((\mathbf{W}v + \mathbf{b})_k, 0) \\ &+ \min((\mathbf{W}u + \mathbf{b})_k, 0)\max((\mathbf{W}v + \mathbf{b})_k, 0) \\ &+ \min((\mathbf{W}u + \mathbf{b})_k, 0)\min((\mathbf{W}v + \mathbf{b})_k, 0) \\ \leq& \max((\mathbf{W}u + \mathbf{b})_k, 0)\max((\mathbf{W}v + \mathbf{b})_k, 0) \\ &+ \min((\mathbf{W}u + \mathbf{b})_k, 0)\min((\mathbf{W}v + \mathbf{b})_k, 0). \end{aligned}$$

Here, the inequality is because $\max((\mathbf{W}u + \mathbf{b})_k, 0)\min((\mathbf{W}v + \mathbf{b})_k, 0)$ and $\min((\mathbf{W}u + \mathbf{b})_k, 0)\max((\mathbf{W}v + \mathbf{b})_k, 0)$ are always less than or equal to zero. Since every element of $\mathbf{W}$ and $\mathbf{b}$ is symmetric (*i.e.*, $\mathbf{W}_{k,l} \overset{d}{=} -\mathbf{W}_{k,l}$ and $\mathbf{b}_k \overset{d}{=} -\mathbf{b}_k$ for $k \in [d_{\text{out}}]$, $l \in [d_{\text{in}}]$), we have

$$\begin{aligned} &\max((\mathbf{W}u + \mathbf{b})_k, 0)\max((\mathbf{W}v + \mathbf{b})_k, 0) \\ &\overset{d}{=} \min((\mathbf{W}u + \mathbf{b})_k, 0)\min((\mathbf{W}v + \mathbf{b})_k, 0), \end{aligned}$$

and thus

$$\begin{aligned} &\mathbb{E}\left[(\mathbf{W}u + \mathbf{b})^T(\mathbf{W}v + \mathbf{b})\right] \\ =& \sum_{k=1}^{d_{\text{out}}} \mathbb{E}\left[(\mathbf{W}u + \mathbf{b})_k(\mathbf{W}v + \mathbf{b})_k\right] \\ \leq& \sum_{k=1}^{d_{\text{out}}} \mathbb{E}\Big[\max((\mathbf{W}u + \mathbf{b})_k, 0)\max((\mathbf{W}v + \mathbf{b})_k, 0) \\ &+ \min((\mathbf{W}u + \mathbf{b})_k, 0)\min((\mathbf{W}v + \mathbf{b})_k, 0)\Big] \\ =& 2\sum_{k=1}^{d_{\text{out}}} \mathbb{E}\left[\max((\mathbf{W}u + \mathbf{b})_k, 0)\max((\mathbf{W}v + \mathbf{b})_k, 0)\right] \\ =& 2\mathbb{E}\left[\phi(\mathbf{W}u + \mathbf{b})^T \phi(\mathbf{W}v + \mathbf{b})\right]. \end{aligned}$$

□

A detailed statement of Theorem 1

Theorem 4 (Monotonicity of cosine similarity)**.** *Suppose $u, v \in \mathbb{R}^{d_{\text{in}}}$ are any two fixed vectors such that $\|u\| = r\|v\|$ for some $r > 0$, $\mathbf{W} \in \mathbb{R}^{d_{\text{out}} \times d_{\text{in}}}$ is a random weight matrix where each element $\mathbf{W}_{k,l} \sim \mathcal{N}(0, d_{\text{out}}^{-1})$ for $k \in [d_{\text{out}}]$, $l \in [d_{\text{in}}]$, and $\mathbf{b} \in \mathbb{R}^{d_{\text{out}}}$ is a random bias vector such that $\mathbf{b}_k \sim \mathcal{N}(0, d_{\text{out}}^{-1})$ for $k \in [d_{\text{out}}]$. If $\cos(u, v) < \left(\frac{1}{2}\left(r + \frac{1}{r}\right)\right)^{-1}$, then the following holds with probability at least $1 - O(1/d_{\text{out}})$.*

$$\cos(\phi(\mathbf{W}u + \mathbf{b}), \phi(\mathbf{W}v + \mathbf{b})) > \cos(u, v).$$

Proof of Theorem 4. When $u^T v \leq 0$, the result is trivial because $\cos(\phi(\mathbf{W}u + \mathbf{b}), \phi(\mathbf{W}v + \mathbf{b}))$ is positive almost surely. Therefore, we only consider the case where $u^T v > 0$.

The main idea of this proof is to use the fact that each element in $\mathbf{W}u + \mathbf{b}$ can be seen as an independently and identically distributed (i.i.d.) copy of some distribution. To be more specific, we first note that for $k \in [d_{\text{out}}]$, due to the Gaussian assumption on $\mathbf{W}$ and $\mathbf{b}$, we have $\sqrt{d_{\text{out}}}(\mathbf{W}u + \mathbf{b})_k \sim \mathcal{N}\left(0, 1 + u^T u\right)$. Then from the definition of a rectified Gaussian distribution[3], we have $\phi(\sqrt{d_{\text{out}}}(\mathbf{W}u + \mathbf{b})_k) \sim \mathcal{N}^{\text{R}}\left(0, 1 + u^T u\right)$. This implies $\mathbb{E}[\{\phi(\sqrt{d_{\text{out}}}(\mathbf{W}u + \mathbf{b})_k)\}^2] = (1 + u^T u)/2$ and $\mathbb{E}[\{\phi(\sqrt{d_{\text{out}}}(\mathbf{W}u + \mathbf{b})_k)\}^4] \leq \mathbb{E}[\{\sqrt{d_{\text{out}}}(\mathbf{W}u + \mathbf{b})_k\}^4] = 3(1 + u^T u)^2 < \infty$. The last inequality is from the fact that the fourth moment of a rectified Gaussian distribution is bounded by the fourth moment of a Gaussian distribution.

[Step 1] For $k \in [d_{\text{out}}]$, we now define T_k as follows

$$T_k := \frac{2}{1 + u^T u}\{\phi(\sqrt{d_{\text{out}}}(\mathbf{W}u + \mathbf{b})_k)\}^2.$$

Note that $T_1, \ldots, T_{d_{\text{out}}}$ are i.i.d. whose mean is one and variance is less than 12. Therefore, by Chebyshev's inequality, for any $\epsilon_1 > 0$

$$\mathbb{P}\left(\left|\frac{1}{d_{\text{out}}}\sum_{k=1}^{d_{\text{out}}} \frac{2\left\{\phi(\sqrt{d_{\text{out}}}(\mathbf{W}u + \mathbf{b})_k)\right\}^2}{1 + u^T u} - 1\right| \geq \epsilon_1\right)$$
$$\leq \frac{12}{d_{\text{out}}\epsilon_1^2} = O\left(\frac{1}{d_{\text{out}}\epsilon_1^2}\right).$$

It is noteworthy that $\frac{1}{d_{\text{out}}}\sum_{k=1}^{d_{\text{out}}}\left\{\phi(\sqrt{d_{\text{out}}}(\mathbf{W}u + \mathbf{b})_k)\right\}^2 = \left\|\phi(\mathbf{W}u + \mathbf{b})\right\|^2$. That is, with probability at least $1 - O(1/(d_{\text{out}}\epsilon_1^2))$, we have

$$\left|\frac{2\left\|\phi(\mathbf{W}u + \mathbf{b})\right\|^2}{1 + u^T u} - 1\right| < \epsilon_1,$$

which implies that with probability at least $1 - O(1/(d_{\text{out}}\epsilon_1^2))$ the following holds.

$$\frac{1}{\left\|\phi(\mathbf{W}u + \mathbf{b})\right\|} > \sqrt{\frac{2}{1 + u^T u}}\left(1 - \frac{\epsilon_1}{2}\right). \tag{2}$$

Similarly, since

$$\phi(\mathbf{W}u + \mathbf{b})^T \phi(\mathbf{W}v + \mathbf{b})$$

[3]For $X \sim \mathcal{N}(\mu, \sigma^2)$, a distribution of a random variable $Y := \max(X, 0)$ is defined as a rectified Gaussian distribution $\mathcal{N}^{\text{R}}(\mu, \sigma^2)$, and it is well known that $\mathbb{E}[Y] = \mu\left(1 - \Psi\left(-\frac{\mu}{\sigma}\right)\right) + \sigma\psi\left(-\frac{\mu}{\sigma}\right)$ and $\text{Var}[Y] = \mu^2\Psi\left(-\frac{\mu}{\sigma}\right)\left(1 - \Psi\left(-\frac{\mu}{\sigma}\right)\right) + \mu\sigma\psi\left(-\frac{\mu}{\sigma}\right)\left(2\Psi\left(-\frac{\mu}{\sigma}\right) - 1\right) + \sigma^2\left(1 - \Psi\left(-\frac{\mu}{\sigma}\right) - \psi\left(-\frac{\mu}{\sigma}^2\right)\right)$. Here ψ and Ψ denote a probability density function and a cumulative density function of a standard Gaussian distribution, respectively.

$$= \frac{1}{d_{\text{out}}} \sum_{k=1}^{d_{\text{out}}} \phi(\sqrt{d_{\text{out}}}(\mathbf{W}u + \mathbf{b})_k)\phi(\sqrt{d_{\text{out}}}(\mathbf{W}v + \mathbf{b})_k),$$

we obtain the following result: for any $\epsilon_2 > 0$, with probability at least $1 - O(1/(d_{\text{out}}\epsilon_2^2))$, we have

$$\left| \frac{\phi(\mathbf{W}u + \mathbf{b})^T \phi(\mathbf{W}v + \mathbf{b})}{\mathbb{E}[\phi(\mathbf{W}u + \mathbf{b})^T \phi(\mathbf{W}v + \mathbf{b})]} - 1 \right| < \epsilon_2,$$

which implies

$$\begin{aligned} &\phi(\mathbf{W}u + \mathbf{b})^T \phi(\mathbf{W}v + \mathbf{b}) \\ &> \mathbb{E}[\phi(\mathbf{W}u + \mathbf{b})^T \phi(\mathbf{W}v + \mathbf{b})](1 - \epsilon_2). \end{aligned} \tag{3}$$

[Step 2] Combining the findings in Equations (2) and (3), for any $\epsilon_1, \epsilon_2 > 0$, with probability at least $1 - O(1/(d_{\text{out}}\epsilon_1^2) - O(1/(d_{\text{out}}\epsilon_2^2))$, we have

$$\begin{aligned} &\cos(\phi(\mathbf{W}u + \mathbf{b}), \phi(\mathbf{W}v + \mathbf{b})) \\ =&\frac{\phi(\mathbf{W}u + \mathbf{b})^T \phi(\mathbf{W}v + \mathbf{b})}{\|\phi(\mathbf{W}u + \mathbf{b})\| \|\phi(\mathbf{W}v + \mathbf{b})\|} \\ >&\mathbb{E}[\phi(\mathbf{W}u + \mathbf{b})^T \phi(\mathbf{W}v + \mathbf{b})] \sqrt{\frac{2}{1 + u^T u}} \sqrt{\frac{2}{1 + v^T v}} \\ &\times \left(1 - \frac{\epsilon_1}{2}\right)^2 (1 - \epsilon_2) \\ \geq&\frac{1 + u^T v}{\sqrt{1 + u^T u}\sqrt{1 + v^T v}} \left(1 - \frac{\epsilon_1}{2}\right)^2 (1 - \epsilon_2). \end{aligned}$$

Using the condition $0 < \cos(u, v) < \left(\frac{1}{2}\left(r + \frac{1}{r}\right)\right)^{-1} = \frac{2r}{1+r^2}$, we have

$$\begin{aligned} &\frac{1 - \cos^2(u, v)}{2r\cos(u, v)\|u\|^2} > 0 > \frac{(1 + r^2)}{2r}\cos(u, v) - 1 \\ \Longrightarrow&1 - \cos^2(u, v) \\ &> (\|u\|^2 + \|v\|^2)\cos^2(u, v) - 2\|u\|\|v\|\cos(u, v) \\ \Longrightarrow&(1 + \cos(u, v)\|u\|\|v\|)^2 \\ &> \cos^2(u, v)(1 + \|u\|^2)(1 + \|v\|^2) \\ \Longleftrightarrow&\frac{1 + u^T v}{\sqrt{1 + u^T u}\sqrt{1 + v^T v}} > \frac{u^T v}{\sqrt{u^T u}\sqrt{v^T v}}. \end{aligned}$$

Therefore, since $\frac{1+u^T v}{\sqrt{1+u^T u}\sqrt{1+v^T v}}$ is strictly greater than $\frac{u^T v}{\sqrt{u^T u}\sqrt{v^T v}}$, by well choosing ϵ such that $\frac{1+u^T v}{\sqrt{1+u^T u}\sqrt{1+v^T v}}(1-\epsilon)^3 > \frac{u^T v}{\sqrt{u^T u}\sqrt{v^T v}}$ and by substituting $\epsilon_1 = 2\epsilon$ and $\epsilon_2 = \epsilon$, we have the following inequality with probability at least $1 - O(1/d_{\text{out}})$.

$$\cos(\phi(\mathbf{W}u + \mathbf{b}), \phi(\mathbf{W}v + \mathbf{b})) > \cos(u, v).$$

□

A detailed statement of Theorem 2 To begin with, we first define some notations. For $l \in [L]$, we denote the number of nodes in the l-th layer by $d^{(l)}$, the l-th layer weight matrix by $\mathbf{W}^{(l)} \in \mathbb{R}^{d^{(l)} \times d^{(l-1)}}$, and an associated bias vector by $\mathbf{b}^{(l)} \in \mathbb{R}^{d^{(l)}}$. We denote the input data by $U \in \mathbb{R}^{d^{(0)}}$. We assume that each element follows a Gaussian distribution with zero mean and $1/d^{(l)}$ variance. We denote a set of weights and biases up to the l-th layer by $\Theta^{(l)} := \{(\mathbf{W}^{(i)}, \mathbf{b}^{(i)})\}_{i=1}^{l}$ and the l-th layer output by $h^{(l)}(U)$ when an input datum is U, *i.e.*, $h^{(l)}(U) = \phi(\mathbf{W}^{(l)} h^{(l-1)}(U) + \mathbf{b}^{(l)})$. We set $h^{(0)}(U) := U$. In the following theorem, we provide a detailed statement of Theorem 2.

Theorem 5 (A detailed statement of Theorem 2)**.** *Let $U \in \mathbb{R}^{d^{(0)}}$ be a random variable for input data with $\|U\| = 1$. We suppose $\mathrm{tr}(\mathrm{Var}[h^{(L-1)}(U) \mid \Theta^{(L-1)}]) = 1 - \beta$. Then, for $k \in [d^{(L)}]$ the following inequality holds.*

$$\frac{\mathrm{Var}[\mathbb{E}[(h^{(L)}(U))_k \mid \Theta^{(L)}]]}{\mathrm{Var}((h^{(L)}(U))_k)} \geq \beta.$$

The relationship between β and the cosine similarity The trace parameter $\beta = 1 - \mathrm{tr}(\mathrm{Var}[h^{(L-1)}(U) \mid \Theta^{(L-1)}])$ captures the cosine similarity of the $(L-1)$-th layer outputs because of the following equality. For independently and identically distributed random variables U_1 and U_2, we have

$$\begin{aligned}
&2\mathrm{tr}(\mathrm{Var}[h^{(L-1)}(U_1) \mid \Theta^{(L-1)}]) \\
&= \mathbb{E}\left[\left\|h^{(L-1)}(U_1) - h^{(L-1)}(U_2)\right\|^2 \mid \Theta^{(L-1)}\right] \\
&\approx 2(1 - \mathbb{E}[\cos(h^{(L-1)}(U_1), h^{(L-1)}(U_2))]).
\end{aligned}$$

The last approximation is due to $\left\|h^{(L-1)}(U_1)\right\| \approx 1$ under the variance conditions on $\mathbf{W}^{(l)}$ and $\mathbf{b}^{(l)}$ (Allen-Zhu et al., 2019, Lemma 7.1). That is, $\mathbb{E}[\cos(h^{(L-1)}(U_1), h^{(L-1)}(U_2))]$ and β are close to each other. It is plausible in practice to assume that β is close to one when the depth L is large because the variance of an intermediate output given $\Theta^{(L-1)}$ is likely to be small due to the cone effect.

Proof of Theorem 5. By the law of total variance, for any $k \in [d^{(L)}]$, we have

$$\frac{\mathrm{Var}[\mathbb{E}[(h^{(L)}(U))_k \mid \Theta^{(L)}]]}{\mathrm{Var}((h^{(L)}(U))_k)} = 1 - \frac{\mathbb{E}[\mathrm{Var}[(h^{(L)}(U))_k \mid \Theta^{(L)}]]}{\mathrm{Var}((h^{(L)}(U))_k)} \tag{4}$$

[Step 1] For $k \in [d^{(L)}]$, a conditional distribution of $(\mathbf{W}^{(L)}h^{(L-1)}(U) + \mathbf{b}^{(L)})_k$ given $\Theta^{(L-1)}$ and U is a Gaussian distribution with zero mean and $(1 + h^{(L-1)}(U)^T h^{(L-1)}(U))/d^{(L)}$ variance, we have

$$\begin{aligned}
&\mathbb{E}[\phi(\mathbf{W}^{(L)}h^{(L-1)}(U) + \mathbf{b}^{(L)})_k]^2 \\
&= \mathbb{E}[\sqrt{1 + h^{(L-1)}(U)^T h^{(L-1)}(U)}]^2/(2\pi d^{(L)}) \\
&\mathbb{E}[\phi(\mathbf{W}^{(L)}h^{(L-1)}(U) + \mathbf{b}^{(L)})_k^2] \\
&= (1 + \mathbb{E}[h^{(L-1)}(U)^T h^{(L-1)}(U)])/d^{(L)},
\end{aligned}$$

and

$$\begin{aligned}
&\mathrm{Var}((h^{(L)}(U))_k) \\
=&\mathbb{E}[\phi(\mathbf{W}^{(L)}h^{(L-1)}(U) + \mathbf{b}^{(L)})_k^2] \\
&- \mathbb{E}[\phi(\mathbf{W}^{(L)}h^{(L-1)}(U) + \mathbf{b}^{(L)})_k]^2 \\
\geq&\frac{(1 + \mathbb{E}[h^{(L-1)}(U)^T h^{(L-1)}(U)])}{d^{(L)}}\frac{\pi - 1}{2\pi}.
\end{aligned} \tag{5}$$

The last inequality is from Jensen's inequality $\mathbb{E}[\sqrt{1 + U^T U}] \leq \sqrt{1 + \mathbb{E}[U^T U]}$.

[Step 2] For $k \in d^{(L)}$, we now consider $\mathbb{E}[\mathrm{Var}[(h^{(L)}(U))_k \mid \Theta^{(L)}]] = \mathbb{E}[\mathrm{Var}[\phi(\mathbf{W}^{(L)}h^{(L-1)}(U) + \mathbf{b}^{(L)})_k \mid \Theta^{(L)}]]$. By the symmetricity of $\mathbf{W}^{(L)}$ and $\mathbf{b}^{(L)}$, we have

$$\begin{aligned}
&\mathbb{E}[\mathrm{Var}[\phi(\mathbf{W}^{(L)}h^{(L-1)}(U) + \mathbf{b}^{(L)})_k \mid \Theta^{(L)}]] \\
&= \frac{1}{2}\mathbb{E}\Big[\mathrm{Var}[\phi(\mathbf{W}^{(L)}h^{(L-1)}(U) + \mathbf{b}^{(L)})_k \mid \Theta^{(L)}] \\
&+ \mathrm{Var}[\phi(-(\mathbf{W}^{(L)}h^{(L-1)}(U) + \mathbf{b}^{(L)}))_k \mid \Theta^{(L)}]\Big].
\end{aligned}$$

Using the characteristic of the ReLU function, we have $\phi(\mathbf{W}^{(L)}h^{(L-1)}(U)+\mathbf{b}^{(L)})_k^2+\phi(-(\mathbf{W}^{(L)}h^{(L-1)}(U)+\mathbf{b}^{(L)}))_k^2=(\mathbf{W}^{(L)}h^{(L-1)}(U)+\mathbf{b}^{(L)})_k^2$ and

$$\begin{aligned}
&\mathbb{E}[\phi(\mathbf{W}^{(L)}h^{(L-1)}(U)+\mathbf{b}^{(L)})_k \mid \Theta^{(L)}]^2 \\
&\quad+\mathbb{E}[\phi(-(\mathbf{W}^{(L)}h^{(L-1)}(U)+\mathbf{b}^{(L)}))_k \mid \Theta^{(L)}]^2 \\
>&\Big(\mathbb{E}[\phi(\mathbf{W}^{(L)}h^{(L-1)}(U)+\mathbf{b}^{(L)})_k \mid \Theta^{(L)}] \\
&\quad-\mathbb{E}[\phi(-(\mathbf{W}^{(L)}h^{(L-1)}(U)+\mathbf{b}^{(L)}))_k \mid \Theta^{(L)}]\Big)^2 \\
=&(\mathbf{W}^{(L)}\mathbb{E}[h^{(L-1)}(U) \mid \Theta^{(L-1)}]+\mathbf{b}^{(L)})_k^2.
\end{aligned}$$

Therefore,

$$\begin{aligned}
&\mathrm{Var}[\phi(\mathbf{W}^{(L)}h^{(L-1)}(U)+\mathbf{b}^{(L)})_k \mid \Theta^{(L)}] \\
&\quad+\mathrm{Var}[\phi(-(\mathbf{W}^{(L)}h^{(L-1)}(U)+\mathbf{b}^{(L)}))_k \mid \Theta^{(L)}] \\
<&\mathbb{E}[(\mathbf{W}^{(L)}h^{(L-1)}(U)+\mathbf{b}^{(L)})_k^2 \mid \Theta^{(L)}] \\
&\quad-(\mathbf{W}^{(L)}\mathbb{E}[h^{(L-1)}(U) \mid \Theta^{(L-1)}]+\mathbf{b}^{(L)})_k^2 \\
&\quad=\mathbf{W}_k^T\mathrm{Var}[h^{(L-1)}(U) \mid \Theta^{(L-1)}]\mathbf{W}_k,
\end{aligned}$$

where $\mathbf{W}_k^T$ is the k-th row of the weight matrix $\mathbf{W}$. Thus, an upper bound for $\mathbb{E}[\mathrm{Var}[(h^{(L)}(U))_k \mid \Theta^{(L)}]]$ is

$$\begin{aligned}
&\mathbb{E}[\mathrm{Var}[\phi(\mathbf{W}^{(L)}h^{(L-1)}(U)+\mathbf{b}^{(L)})_k \mid \Theta^{(L)}]] \\
&<\frac{1}{2}\mathbb{E}[\mathbf{W}_k^T\mathrm{Var}[h^{(L-1)}(U) \mid \Theta^{(L-1)}]\mathbf{W}_k] \\
&=\frac{1}{2}\mathrm{tr}(\mathrm{Var}[h^{(L-1)}(U) \mid \Theta^{(L-1)}])/d^{(L)}.
\end{aligned} \tag{6}$$

[Step 3] Finally, combining Equations (5) and (6)

$$\begin{aligned}
&\frac{\mathbb{E}[\mathrm{Var}[(h^{(L)}(U))_k \mid \Theta^{(L)}]]}{\mathrm{Var}((h^{(L)}(U))_k)} \\
&<\frac{\mathrm{tr}(\mathrm{Var}[h^{(L-1)}(U) \mid \Theta^{(L-1)}])}{1+\mathbb{E}[h^{(L-1)}(U)^Th^{(L-1)}(U)]}\frac{\pi}{\pi-1} \\
&<1-\beta.
\end{aligned}$$

The last inequality is due to the fact $\mathbb{E}[h^{(L-1)}(U)^Th^{(L-1)}(U)]=1$ when $\|U\|=1$ and $\pi<2(\pi-1)$. Due to Equation (4), it concludes a proof. □